CHEMISTRY OF MATERIALS
Cite This: Chem. Mater. 2019, 31, 10225−10235
Article
pubs.acs.org/cm

Stabilizer-Free CuIr Alloy Nanoparticle Catalysts†

Hongyu Guo,‡ Hao Li,‡ Desiree Fernandez,‡ Scott Willis,‡,∥ Karalee Jarvis,§ Graeme Henkelman,*,‡ and Simon M. Humphrey*,‡

‡Department of Chemistry, The University of Texas at Austin, Welch Hall 2.204, 105 East 24th Street Stop A5300, Austin, Texas 78712-1224, United States

§Texas Materials Institute, The University of Texas at Austin, 204 East Dean Keeton Street Stop C2201, Austin, Texas 78712-1591, United States

Supporting Information

ABSTRACT: We present the direct synthesis of stabilizer-free Cu−Ir alloy nanoparticles (NPs) with tunable compositions. Cu and Ir are classically immiscible in the bulk. Therefore, the physical and catalytic properties of Cu−Ir alloys are largely unknown. A convenient microwave-assisted method utilizes readily available Cu^{2+} salts and $IrCl_3$ in a modified polyol reaction; NaOH facilitates rapid solvent-assisted coreduction to yield $Cu_xIr_{(100-x)}$NPs, where x can be varied within the approximate range 10−50. The as-synthesized NPs form stable dispersions of small (∼2 nm) and near-monodisperse cuboctahedra without the requirement of organic stabilizing (capping) agents, resulting in nanostructures that are directly amenable to heterogeneous catalysis. $Cu_xIr_{(100-x)}$NPs supported on mesoporous Co_3O_4 show high selectivity toward the selective partial hydrogenation of crotonaldehyde to yield >40% crotyl alcohol in the vapor phase. The selectivity toward C═O versus C═C bond hydrogenation is largely insensitive to the Cu:Ir ratio but more Ir rich compositions are also more highly active. Density functional theory (DFT) studies explain this behavior in two ways: first the Co_3O_4 support enhances selective C═O bond activation of the crotonaldehyde feedstock via favorable support-reagent adsorption; second, increasingly Ir-rich CuIrNP surfaces provide more Ir- sites, resulting in higher hydrogenation activity.

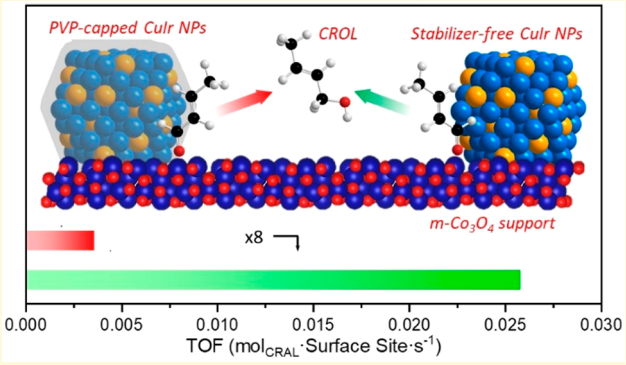

INTRODUCTION

The synthesis and chemistry of nanoscale bimetallic solid-solutions of a noble metal and a first-row transition metal are of topical interest for applications in catalysis,[1−3] optics,[4,5] and sensing.[6,7] Partial substitution of noble metal atoms in their native face-centered cubic (FCC) crystalline lattices with cheaper, more abundant first-row transition metals is a convenient way to reduce their overall volumetric cost. Simultaneously, alloying can lead to enhanced chemical and thermal stability compared with the pure noble metals. Furthermore, from the perspective of surface chemistry and catalysis, the average binding energy of an alloy surface toward reactant molecules can be fine-tuned as a function of both electronic (i.e., *d*-band center) and geometric (i.e., surface ensemble) effects that arise from local heteroatomic interactions. Control of such effects can be achieved via synthetic control over an alloy's composition and structure. In turn, this general strategy can permit substantial catalytic activity and selectivity enhancements for noble metal catalysts commonly utilized in large-scale chemical conversions, whose properties have otherwise already been fully optimized.[8−10]

Many approaches have been developed to prepare alloy NPs of noble metals and light transition metals, such as chemical coreduction[11−13] and thermolysis.[14,15] Microwave-assisted methods have proven to be efficient in generating alloy NPs with well-defined compositions and structural homogeneity.[16−18] Under microwave irradiation, polar solvent molecules and other polarizable precursors (e.g., metal ions) undergo dipolar rotational excitation, leading to rapid and localized heat dissipation. As a result, inhomogeneous heat transfer leads to the formation of short-lived "hot-spots", whose temperatures can be orders of magnitude higher than the bulk solution.[19,20] Within these regions, metal precursors of classically immiscible systems may be reduced and coincorporated into nanoparticle seeds as metastable solid-solution alloys.[16,21,22] For example, we have shown in our previous studies that RhAg and AgIr alloy NPs can be formed using microwave heating while conventional heating under otherwise identical conditions generates ill-defined mixtures of predominantly monometallic NPs.[21,22]

In general, solvent-based routes for the synthesis of well-defined metallic NPs requires the presence of stabilizers (a.k.a.

Received: October 9, 2019
Revised: November 22, 2019
Published: November 25, 2019

DOI: 10.1021/acs.chemmater.9b04138
Chem. Mater. 2019, 31, 10225−10235

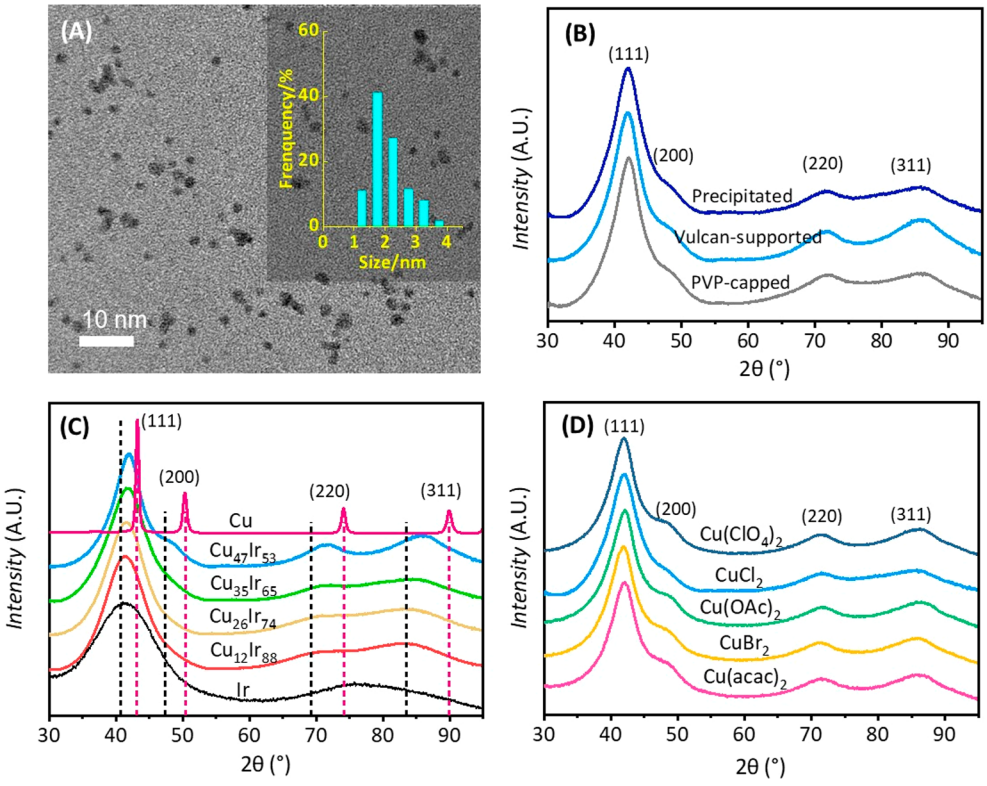

Figure 1. (A) TEM image of as-synthesized $Cu_{47}Ir_{53}$NPs; Inset: size distribution histography. (B) PXRD patterns of PVP-capped, Vulcan-supported and precipitated $Cu_{47}Ir_{53}$NPs. (C) PXRD patterns of Vulcan-supported Cu, Ir, and CuIrNPs with different compositions. The corresponding theoretical reflection positions for Cu (JCPDS card # 04−0836) and Ir (JCPDS card # 006−0598) are also shown for reference. (D) PXRD patterns for $Cu_xIr_{(100-x)}$NPs with Ir nominal composition 50% prepared with different Cu precursors.

capping agents) that adhere to the growing NP surfaces via weak to moderately strong covalent or ionic interactions. Stabilizers are often critical to prevent particle-to-particle agglomeration, as well as to control the rate and/or direction of further NP growth.[23,24] Common capping agents include organic polymers (e.g., *poly*(vinylpyrrolidone) (PVP), *poly*(-vinyl alcohol) (PVA)), and organic molecules or ions (e.g., oleylamine, citrate).[23] Unfortunately, however, from the perspective of heterogeneous catalysis, any such capping agent represents an intrinsic hindrance to the final application: surface-bound stabilizers serve to block metal surface sites from reactant molecules, thus resulting in slow catalytic turnover. Furthermore, removal of capping agents prior to catalysis often requires relatively harsh chemical or physical treatments, which can inadvertently cause unwanted restructuring (i.e., morphological changes or dealloying) of the NP catalysts.

Methods to remove capping agents from the surfaces of NPs, such as thermal annealing,[25−28] UV-ozone treatment,[29−31] or chemical treatment[32−37] can result in unwanted surface oxidation, structure, or shape change of alloy noble metal NPs.[38,39] Incomplete decomposition of organic capping agents can also result in surface coking and/or poisoning, which can retard catalytic performance.[40] Thus, identifying new ways to prepare well-defined metallic nanocatalysts that do not require bulky or strongly bound surface stabilizers is of topical interest.[41−43] For example, Xia and co-workers showed that the total amount of oleic acid and oleylamine capping agents required to stabilize Pt−Ni NPs could be reduced using benzyl ether as a solvent and competitive stabilizer; this resulted in a significant electrocatalytic enhancement in the oxygen reduction reaction versus Pt−Ni NPs with higher oleic acid/oleylamine surface coverage.[44]

Here, we present a rapid and convenient microwave-assisted method for the preparation of CuIrNPs without the use of traditional stabilizers. The NPs are only stabilized by the solvent (ethylene glycol; EG) and weakly bound chloride ions from the precursors. The method provides near-monodisperse and ultrasmall (ca. 2 nm) CuIrNPs as stable suspensions. The NPs can be easily dispersed onto different inorganic supports and are highly active in selective hydrogenation reactions in the vapor-phase without the requirement for any pretreatment. In 2018, we published the first example of Ag−Ir alloy NPs prepared by a microwave-assisted method.[21] At around the same time, the Kitagawa group in Kyoto published the first example of Cu−Ir alloy NPs, prepared by a conventional method.[45] Arguably, the use of Cu in place of Ag is more attractive from an economic standpoint in terms of bulk catalyst synthesis. Notably, however, both of these prior works required the presence of PVP as a capping agent. We were therefore motivated to further investigate the synthesis of Cu−Ir nanostructures in the absence of PVP.

RESULTS AND DISCUSSION

$Cu_xIr_{(100-x)}$NPs with defined compositions were prepared by changing the relative molar amounts of the Cu^{2+} and Ir^{3+} precursors employed. A single solution containing both $CuCl_2 \cdot 2H_2O$ and $IrCl_3 \cdot xH_2O$ premixed in EG was injected directly into a stirred EG solution containing NaOH (0.0125 M), which was preheated to 125 °C inside the cavity of a CEM-MARS-5 microwave reactor under a flowing atmosphere of N_2 gas. The precursors were then added at a rate of 0.4 $mmol_{Cu+Ir}$

DOI: 10.1021/acs.chemmater.9b04138
Chem. Mater. 2019, 31, 10225−10235

h^{-1} over a 15 min injection period, controlled by syringe pump (see Supporting Information, SI, for further details). Almost instantly upon initiation of the precursor injection, a dark suspension was formed, indicative of rapid reduction of the metal precursors. The suspensions were heated for an additional 30 min at 125 °C before being quenched in an ice water bath. The resulting NPs were stable upon standing indefinitely in the EG mother liquor upon exposure to air. In actuality, the EG solvent should itself be regarded as a surface passivation agent, since it has the capability to form weak donor−acceptor interactions with atoms on the NP surfaces via the EG-oxygen lone pairs. However, EG is known to act as a very weakly coordinating solvent in both molecular and heterogeneous settings, and is competitively desorbed from NP surfaces in the presence of species bearing stronger (i.e., more Lewis basic) donors. Since there is likely no such thing as "naked" NPs in solution, it can be assumed that EG acts to stabilize the ultrasmall NPs prepared by this method (vide infra).

In order to determine the range of alloy compositions that could be accessed by this method, a systematic series of reactions were conducted to prepare $Cu_xIr_{(100-x)}$NPs with different nominal target compositions in the range x = 10−90. The isolated NPs were initially analyzed by a combination of transmission electron microscopy (TEM) to determine average size, morphology and dispersity, and by powder X-ray diffraction (PXRD) to determine the bulk atomic structure and extent of alloying. For the TEM studies, the as-synthesized NPs in EG were diluted by addition of ethanol (ca. 1:15 v/v) and directly drop-cast on to Formvar-coated grids. In support of the premise that EG acts to stabilize the CuIrNPs, direct drop-casting of the as-synthesized NPs on to Formvar-coated grids and subsequent imaging by TEM revealed well-dispersed and near-monodisperse 1.7−2.1 nm CuIrNPs, without evidence of any agglomeration (Figures 1A and S1).

Since PXRD requires the isolation of solid (dry) samples, a number of isolation methods were tested. First, the as-synthesized NPs were subjected to precipitation by addition of acetone followed by centrifugation. Indexing of the observed reflections confirmed that the CuIrNPs adopted a face-centered cubic (FCC) structure as for the individual metals (Figure 1B). The solid material isolated by this method could not be readily redispersed in fresh EG upon sonication. This observation suggested to us that the NPs had become irreversibly agglomerated (Figure S2). While perhaps this was an unsurprising result, this was not a prohibitive issue since our intention was to directly support the stabilizer-free CuIrNPs on to secondary catalyst supports via incipient wetness impregnation. This step circumvents agglomeration issues while simultaneously providing catalysts with clean metal surfaces. As an alternative preparation method that more closely mirrors the desired catalyst preparation method, we next prepared PXRD samples by addition of amorphous graphitic carbon (Vulcan XC-72R) to the as-synthesized CuIrNP solutions (to achieve an approximate 30 wt % total metal loading) followed by overnight stirring under N_2. Subsequent isolation of the CuIrNP-Vulcan composites by vacuum filtration, washing with ethanol and drying the samples under vacuum gave free-flowing powders whose PXRD patterns were indistinguishable from the directly centrifuged samples (Figure 1B). Third, the as-synthesized CuIrNP suspensions were treated by the direct addition of solid PVP followed by stirring at room temperature for 10 min, followed by precipitation with acetone and centrifugation. This yielded a glassy solid, reminiscent of what is usually obtained when PVP is included in the NP synthesis. The resulting PXRD patterns of this material were indiscernible from the other methods of isolation (Figures 1B and S3) but the NPs could be readily redispersed into fresh EG solvent. Taken together, these analytical results and qualitative observations suggest that EG does indeed function as a weak stabilizing agent for the CuIrNPs, and is easily displaced by precipitation or by the introduction of more effective capping agents.

Direct comparisons of the PXRD patterns obtained on Vulcan (Figure 1C) or via the addition of PVP (Figure S3) as a function of relative Cu:Ir ratios employed in the precursor solutions showed that the positions of the (111) and (220) reflections for the $Cu_xIr_{(100-x)}$NPs were located between the indexed positions corresponding to pure Cu and Ir standards from the database, indicative of intrinsic alloying between Cu and Ir. Furthermore, a consistent shift was observed in line with the value of x (Figures 1C and S4−S6). In general, all reflections were broad, as expected for very small NPs. In line with the TEM measurements, the most Ir-rich CuIrNPs gave the broadest X-ray reflections, and correspond to the smallest average NP diameters. The $Cu_xIr_{(100-x)}$NP sizes were also predicted from the PXRD data using the Scherrer equation, which showed a consistent increase in size with increasingly higher Cu composition (Table 1).

Table 1. Physical Characterization of $Cu_xIr_{(100-x)}$NPs

nominal composition (%)		size (nm)		composition by ICP-OES (%)		composition by XPS (%)	
Cu	Ir	PXRD	STEM	Cu	Ir	Cu	Ir
12	88	1.1	1.74 ± 0.49	12	88	12	88
25	75	1.5	1.84 ± 0.45	26	74	26	74
38	62	1.8	2.00 ± 0.63	35	65	34	65
50	50	2.1	2.10 ± 0.55	47	53	46	54

Using the microwave-assisted method described above, the PXRD patterns of increasingly Cu-rich $Cu_xIr_{(100-x)}$NPs (x > 47) showed the evolution of asymmetric reflections with shoulders at lower 2θ values, indicative of the presence of pure CuNPs in addition to CuIr alloys (Figure S7). Correspondingly, TEM imaging revealed a bimodal distribution of particle sizes, with the presence of additional, larger (>20 nm) monometallic CuNPs (confirmed by energy-dispersive spectroscopy (EDS); Figure S8). The apparent inability of the microwave method to form Cu-rich alloys is likely due to differences in the comparative reduction rates of Cu^{2+} and Ir^{3+} in EG. Ir^{3+} is reduced faster than Cu^{2+} under the reaction conditions; therefore, higher Cu^{2+} concentrations are likely to favor spontaneous nucleation of CuNPs, which in turn disfavors the incorporation of Cu^{2+} ions into the growing CuIr nuclei.[46] We have observed similar behavior in the case of AgIrNPs.[21] Kitagawa and co-workers were able to prepare a wider range of PVP-capped CuIrNPs, albeit at a significantly higher reaction temperature (T = 225 °C *c.f.* 125 °C), which may have facilitated faster Cu^{2+} reduction.[45]

$Cu_xIr_{(100-x)}$NPs with $x \approx$ 10−50 could also be prepared using a broad range of other common Cu^{2+} precursors. The PXRD patterns of CuIrNPs prepared from four different common Cu^{2+} precursors ($Cu(ClO_4)_2{\cdot}6H_2O$, $Cu(OAc)_2{\cdot}H_2O$, $CuBr_2$, $Cu(acac)_2$) with a nominal $Cu_{50}Ir_{50}$ composition

DOI: 10.1021/acs.chemmater.9b04138
Chem. Mater. 2019, 31, 10225−10235

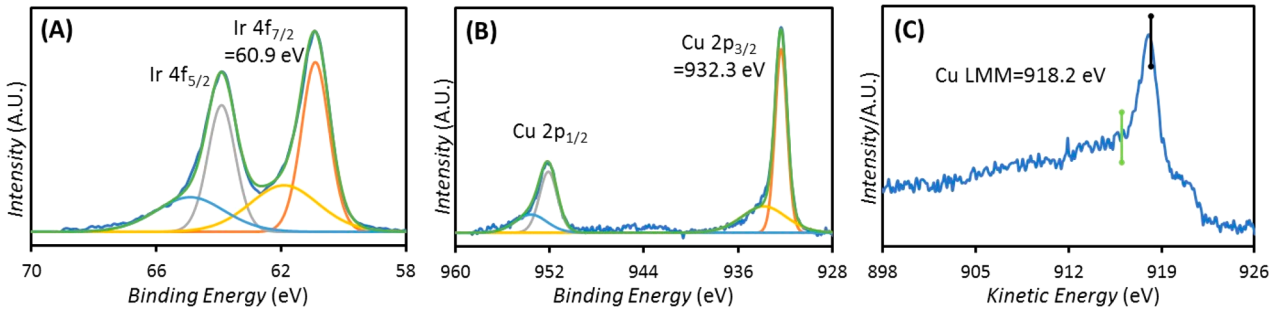

Figure 2. Deconvoluted XPS spectra of (A) Ir 4f region (B) Cu 2p region and (C) Cu LMM Auger for $Cu_{47}Ir_{53}$ NPs, with references shown in solid lines (black: Cu(0); green: Cu(I)); the binding energies were referenced to C 1s graphite (284.5 eV).

showed the same diffraction patterns to that of $Cu_{50}Ir_{50}$NPs prepared using $CuCl_2{\cdot}2H_2O$ (Figure 1D).

To assess the actual final compositions of the as-synthesized CuIrNPs in this work, inductively coupled plasma optical emission spectroscopy (ICP-OES) and X-ray photoelectron spectroscopy (XPS) were employed (Table 1). Samples were prepared for ICP-OES and XPS by directly depositing the CuIrNPs on Vulcan carbon; for the former analysis, the CuIrNP-Vulcan composites were digested by heating to 200 °C in a concentrated aqueous HCl/H_2O_2 solution to effect complete dissolution. For all compositions studied, there was excellent agreement between the measured Cu:Ir ratios by ICP-OES and XPS, and the measured values were also close to the nominal compositions, indicating that the Cu^{2+} and Ir^{3+} precursors were fully reduced and incorporated into CuIrNPs during the syntheses.

The XPS characterizations also revealed further important information regarding the distribution of surface oxidation states of the CuIrNPs. The measured binding energies for Cu and Ir were referenced to C 1s from graphite (284.5 eV). The XPS spectrum for $Cu_{47}Ir_{53}$NPs gave emission bands ca. 63.9 and 60.9 eV, corresponding to the $4f_{5/2}$ and $4f_{7/2}$ transitions for Ir.[47] Peak deconvolution indicated that approximately 70% was Ir^0 and the remaining 30% was Ir^{4+} (Figure 2A). The Cu 2p region of the spectrum showed a similar ratio of $Cu^{0/+}$:Cu^{2+} of 70:30, which was also confirmed by the presence of low-intensity satellite peaks (Figure 2B). Since Cu^0 and Cu^+ both have identical binding energies of 932.3 eV, differentiating these two oxidation states is difficult. However, the Cu LMM Auger line with a kinetic energy of 918.2 eV confirmed that most of the copper in $Cu_xIr_{(100-x)}$NPs was in fact in the zerovalent metallic state (Figure 2C). Given the average measure size of the $Cu_{47}Ir_{53}$NPs (2.10 nm) and assuming a cuboctahedral morphology, an average NP consisting of 309 total atoms would present 52% of the atoms at the surface. The XPS findings here suggest that all core Cu and Ir atoms are in the metallic state, while the surfaces are presumably composed of a mixture of oxidation states, due to partial surface oxidation. Increasingly Ir-rich CuIrNPs showed similar XPS-derived ratios of oxidation states to that of $Cu_{47}Ir_{53}$, and no obvious binding energy shifts were observed due to compositional differences (Figures S9−12 and Table S1).

High-angle annular dark field scanning transmission electron microscopy (HAADF-STEM) images of various $Cu_xIr_{(100-x)}$NPs further confirmed that the majority of NPs adopted a spherical shape (Figure 3A−E). Size measurements of >300 particles of a given composition showed that the average $Cu_xIr_{(100-x)}$NP diameter had a liner dependence with composition, with the most Cu-rich NPs being the largest

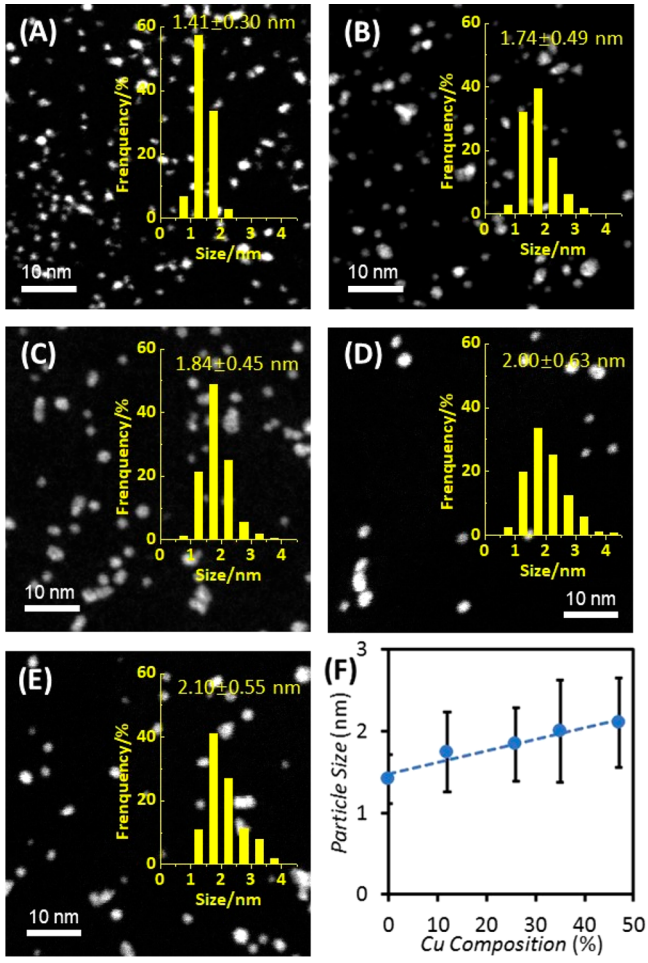

Figure 3. HADDF-STEM images for stabilizer-free NPs: (A) pure IrNPs; (B) $Cu_{12}Ir_{88}$NPs; (C) $Cu_{26}Ir_{74}$NPs; (D) $Cu_{35}Ir_{65}$NPs; (E) $Cu_{47}Ir_{54}$ NPs; and (F) particle size as a function of Cu composition. The insets show the corresponding size distribution histographs.

(Figure 3F). The NP sizes obtained from HAADF-STEM imaging were also consistent with the results of the Scherrer equation (Table 1). Pure Cu NPs prepared by the same method have a much larger size (>50 nm) and wider size distribution (Figure S13). 2D EDS elemental mapping analysis of a collection of three $Cu_{47}Ir_{53}$NPs further confirmed homogeneous mixing of Cu and Ir at the nanoscale, verifying a uniform solid-solution alloy structure within the CuIrNPs (Figure S14).

As mentioned above, the stabilizer-free CuIrNPs remained dispersed in the EG mother liquor without undergoing

DOI: 10.1021/acs.chemmater.9b04138
Chem. Mater. 2019, 31, 10225−10235

Scheme 1. Most Commonly Obtained Reaction Outcomes in the Hydrogenation of Crotonaldehyde

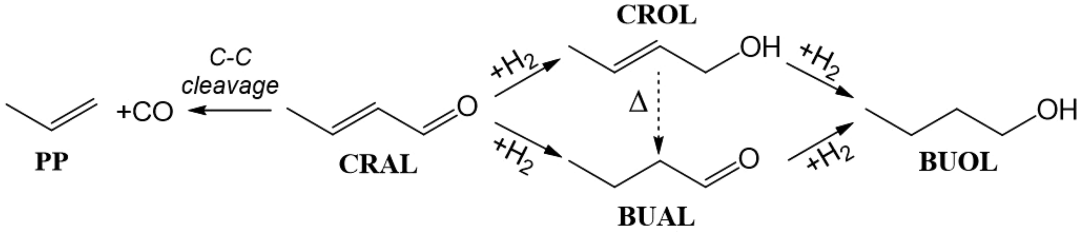

precipitation for weeks. This infers that the NP surfaces were protected by adsorbates present in, or generated by, the synthetic method. Attempts were made to probe the identity of the species acting as stabilizers. Previously, Kunz and co-workers studied the surface chemistry of capping agent-free Pt nanoclusters obtained by conventional methods.[48] FT−IR spectroscopy was employed to identify the presence of CO ligands bound at the PtNP surfaces, generated in situ by solvent decarbonylation. The C≡O stretching frequencies were found to be sensitive to the OH^- concentration, which led to the conclusion that the PtNPs were stabilized by both CO and OH^-. Accordingly, we studied the CuIrNPs by FT−IR spectroscopy but did not detect any CO moieties at the CuIrNP surfaces (Figure S15). Presumably, either CO was not generated under the microwave-assisted reaction conditions, or its surface adsorption was disfavored at the Cu−Ir alloy surfaces. However, it is reasonable to assume that OH^- from NaOH could act as a stabilizing agent, as could Cl^- ions released from the $CuCl_2$ and $IrCl_3$ precursors. A closer examination of the XPS spectrum of the as-synthesized CuIrNPs deposited on to Vulcan carbon confirmed the presence of Cl (Figure S16), with an atomic ratio of Cl:Ir = 1:10. In order to rule out the physisorption of Cl^- on the carbon support, an XPS spectrum was also taken of Vulcan carbon after exposure to a solution of NaCl containing the same molar quantity of Cl^- as in the CuIrNP synthesis. No Cl signal was observed in this case, indicating that the Cl detected in the CuIrNPs-Vulcan composites was predominantly associated with the NPs (Figure S16). Thus, it is most likely that the CuIrNPs prepared in this work are electrostatically stabilized by a combination of Cl^- and OH^- adsorbates in addition to steric stabilization by EG. Furthermore, the as-synthesized CuIrNPs were rapidly precipitated by the addition of large quantities of other electrolytes (e.g., NaOH, H_2SO_4, Na_2SO_4). Once precipitated, the solid could not be redispersed into fresh solvent, including H_2O, EtOH, EG, acetone, DMF, or THF.

In order to understand the role of NaOH in the synthesis of CuIrNPs, attempts were also made to prepare Cu, Ir, and CuIrNPs in the absence of NaOH. Without NaOH, the reduction of $IrCl_3$ by EG demands temperature equal to or higher than 150 °C, while the reduction of Cu(II) could not be achieved even after heating the EG solution of Cu(II) to boiling point for 1 h. This is mainly due to the low standard reduction potential of Cu^{2+}/Cu^0 (0.34 V) compared with Ir^{3+}/Ir^0 (1.16 V).[49] Interestingly, when an equimolar mixture of $CuCl_2$ and $IrCl_3$ was added to EG preheated at 150 °C, Cu^{2+} could be partially reduced (possibly due to autocatalytic reduction by IrNPs);[50,51] the bulk NP composition was determined to be $Cu_{18}Ir_{82}$ by both ICP-OES and XPS. However, increasing the reaction temperature or changing the precursor ratios did not achieve a further increase in the relative Cu composition (Figures S17−S19). It has been reported that NaOH promotes the dehydration of EG at elevated temperature, generating H_2O and acetaldehyde.[52,53] The latter, being a stronger reducing agent than EG, is believed to facilitate the reduction of metal precursors (especially Cu(II)) at lower temperature and promote the formation of solid-solution alloy structures over a broader composition range.

To study the catalytic properties of CuIrNPs, vapor-phase hydrogenation of crotonaldehyde (CRAL) was chosen as a model reaction, since it allows both the catalytic turnover and the C═O versus C═C hydrogenation selectivity to be simultaneously assessed as a function of the alloy composition. The heterogeneous hydrogenation of CRAL by H_2 gas provides a number of product outcomes, which are summarized in Scheme 1. Selective hydrogenation of the C═O bond to yield crotyl alcohol (CROL) is the industrially desired product, but hydrogenation of the C═C bond to yield butyraldehyde (BUAL) is thermodynamically favored, while CROL is kinetically unstable with respect to rearrangement to yield BUAL.[54] As such, this continues to be a challenging reaction of both fundamental and practical interest. Secondary support effects are widely known to play a crucial role in enhancing the reaction selectivity to yield CROL via activation of the C═O bond.[55,56] Recent works by our group[21] and Somorjai group[56] have shown that amorphous and mesoporous forms of Co_3O_4 provide enhanced selectivity toward CROL, due to preferential head-on adsorption of CRAL with the Co_3O_4 surface via support···O═C(H)CH═$CHCH_3$ interactions that destabilize the C═O bond and promote hydride transfer to these groups.[56] Meanwhile, direct adsorption of CRAL at the metal NP surfaces has been shown to favor activation of the C═C bond via thermodynamically more favorable side-on binding; modification of a Cu(111) surface with adatoms such as S have been shown to force the CRAL to tilt, resulting in increased C═O activation.[57]

In this work, catalysts were prepared by direct mixing of the as-synthesized $Cu_xIr_{(100-x)}$NP suspensions with dispersion of mesoporous (*m*-) Co_3O_4 in EtOH and stirring for 24 h (see SI). The composites were separated by centrifugation and washed by EtOH before being dried under vacuum at room temperature. The actual metal loadings achieved by this method were determined by ICP-OES. In a typical catalytic study, 30 mg of the supported catalyst was mixed with acid-washed sand and placed on a D3 porosity frit in a custom-made single-pass quartz reactor. The $Cu_xIr_{(100-x)}$/*m*-Co_3O_4 catalysts were stabilized under the reaction conditions in the absence of CRAL under flowing H_2/He at 70 °C for 1 h. To initiate the catalysis, CRAL vapor was then introduced into the gas flow using a fritted bubbler held at 0 °C to ensure the vapor pressure remained constant. Products were monitored

DOI: 10.1021/acs.chemmater.9b04138
Chem. Mater. 2019, 31, 10225−10235

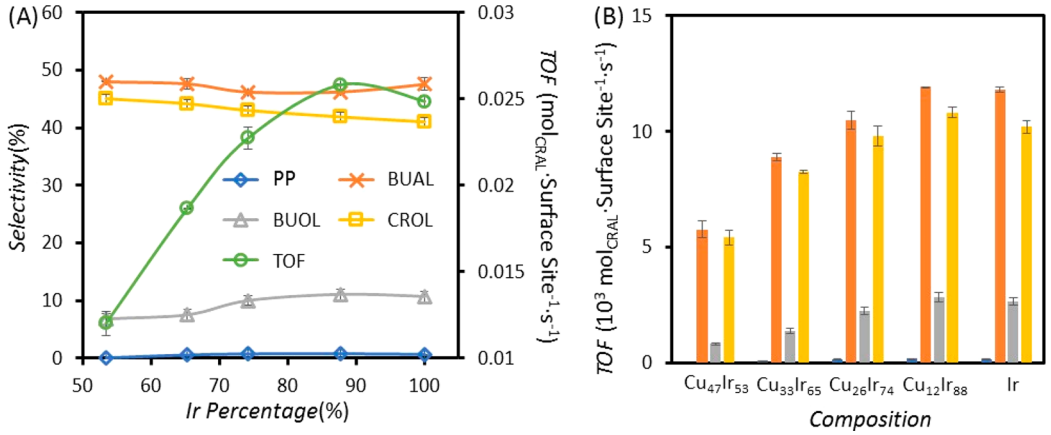

Figure 4. (A) The selectivity to propene (blue), butyraldehyde (orange), butanol (gray), crotyl alcohol (yellow), and turnover frequency (green) obtained on $Cu_xIr_{(100-x)}/m$-Co_3O_4, as a function of Ir percentage. (B) The turnover frequency to corresponding products obtained on $Cu_xIr_{(100-x)}/m$-Co_3O_4 with different composition.

on-stream by a gas chromatograph (GC) fitted with an autosampler and using flame ionization detection (FID). Turnover frequencies (TOFs; mol_{CRAL}/surface site/s) were calculated by taking the corrected raw FID integrations, applying correction factors, and by estimation of the total metal surface sites from the TEM data (see SI for details).

The TOF and product selectivity data obtained for five separate m-Co_3O_4-supported catalysts with different Cu:Ir compositions ($Cu_{47}Ir_{53}$ $Cu_{35}Ir_{65}$, $Cu_{26}Ir_{74}$, $Cu_{12}Ir_{88}$, Ir_{100}) is summarized in Figure 4; the data points reflect TOF and selectivity values for the catalysts after 140 min on-stream, at which point the catalysts had reached a pseudosteady-state. The first observation is that the overall catalyst activity toward CRAL hydrogenation smoothly increased as a function of increasing Ir content, and reached a maximum at $Cu_{12}Ir_{88}$; pure IrNPs of the same size were slightly less active than the most Ir-rich alloy (Figure 4A; green data). Second, all catalysts produced over 40% of the target CROL and a similar amount of BUAL (Figure 4A; yellow and orange data); this extent of selectivity toward CROL is comparable to the best reported Ir catalysts in the literature.[58] It should be noted that the same NP catalysts supported on amorphous SiO_2 produced only BUAL and no CROL under the same reaction conditions (Figure S20). This is direct evidence that the m-Co_3O_4 support plays an important role in activation of the C═O bond in CRAL (see above), and is further supported by the observation that the relative selectivities toward CROL and BUAL were largely insensitive to the Cu:Ir ratio. More specifically, the amount of the target CROL produced smoothly and gradually decreased from 45 to 41% with increasing Ir content, which also corresponds to an increasing overall TOF_{CRAL} in line with previous observations that more Ir-rich NPs favor direct C═C hydrogenation at the NP surfaces. A minority of doubly hydrogenated BUOL was also observed for all compositions, which also increased to ca. 10% for the most Ir-rich catalysts. Detectable trace amounts of propylene (PP; < 0.5%) were also detected for all catalysts (Figure 4A). The TOF values for BUAL, CROL, and BUOL as a function of the Cu:Ir ratio are shown in Figure 4B.

Given the fact that the CuIrNPs are electrostatically stabilized, we investigated the role that Cl^- ions at the NP surfaces may play in blocking surface sites. Unlike the range of common Cu(II) salt precursors that are commercially available, chloride precursors of Ir(III) are by far the most favored from an industrial perspective, as they are most widely available at a reasonable cost. Organometallic Ir precursors are often less soluble in EG and are commonly the Ir(I) salts, which detrimentally change the reduction kinetics. As such, to probe the potential role of Cl ligands upon catalytic activity, we used the same synthesis method to prepare analogous $Cu_{15}Ir_{85}$NPs using halide-free $Cu(TFA)_2$ and $Ir(TFA)_3$ precursors. TEM analysis confirmed the NPs were similar in size and dispersity to the Cl-based NPs (Figure S21) and ICP-OES was used to confirm the Cu:Ir composition in bulk (Table S2). The TFA-$Cu_{15}Ir_{85}$NPs were dispersed on Vulcan carbon as described above; XPS analysis confirmed no Cl was present but a new signal corresponding to the presence of F (1s) was also found, which confirmed the presence of TFA ligands (Figure S22). Interestingly, the catalytic activity of this catalyst was the same as the corresponding Cl-stabilized catalyst within experimental error (Figure S23).

TFA ($F_3CCO_2^-$) is known to be a more weakly binding stabilizer than Cl^- in both homogeneous and heterogeneous settings; it is a weak conjugate base of the corresponding acid.[59] The experimental ratio of $F_3CCO_2^-$:Ir = 1:14, while for the Cl-based CuIrNPs, the ratio of Cl:Ir was 1:10. The lower amount of TFA on the NP surfaces may be due to weaker binding of TFA or steric considerations. Considering there is an equal amount of Cu and Ir in the NPs, and ∼52% of the metal atoms are on the outermost layer of an average NP consisting of 309 atoms, the ratio of Cl^- and CF_3COO^- to surface metal atoms is 1:10.4 and 1:14.6, respectively. Collectively, we conclude that the Cl^- ligands do not play a major role in hampering the catalytic ability of the NPs.

We also compared the catalytic activities of PVP-capped CuIrNPs versus the capping agent-free NPs by taking a batch of the most active catalyst composition, $Cu_{12}Ir_{88}$, and adding PVP to the NP solution after synthesis. The PVP-capped $Cu_{12}Ir_{88}$NPs were then deposited on m-Co_3O_4 and ICP-OES and TEM were used to confirm comparative loading behavior (Figure S24). Without pretreatment, the purposely PVP-capped catalyst possessed a TOF of 0.0036 mol_{CRAL}·surface site^{-1}·s^{-1}, which was only one-eighth of that for its capping agent-free counterpart (0.0258 mol_{CRAL}·surface site^{-1}·s^{-1}).

Next, density functional theory (DFT) calculations were conducted to provide a more in-depth understanding of the observed experimental catalytic properties as a function of Cu:Ir compositions. It has been shown in previous studies that

DOI: 10.1021/acs.chemmater.9b04138
Chem. Mater. 2019, 31, 10225−10235

the tunability of the H binding energy on bimetallic alloy surfaces is the most important descriptor of hydrogenation activity.[22,39,60−62] Therefore, DFT calculations were first used to calculate the H binding energies on $Cu_xIr_{(1-x)}$ (x = 0.25, 0.50, and 0.75) (111) alloy surfaces (Figure 5A). Except for

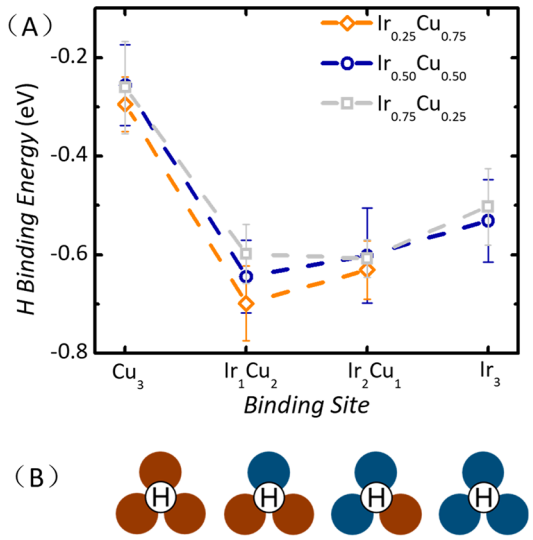

Figure 5. (A) DFT-calculated H binding energies at four different triatomic ensembles on CuIr surfaces. Each error bar represents the standard deviation of ten calculated H binding energies. Ten random configurations of Cu_xIr_{1-x} were generated for calculations. (B) Schematic pictures of H binding sites at the four different triatomic ensembles after DFT relaxation. Blue and brown circles represent Ir and Cu atoms, respectively.

Cu_3 triatomic ensembles, the other three Ir-related triatomic ensembles (Ir_1Cu_2, Ir_2Cu_1, and Ir_3) all have relatively strong average H binding energies; Ir_1Cu_2 tends to have the strongest H binding, followed by Ir_2Cu_1 and Ir_3 (Figure 5A). Interestingly, for the $Ir_{0.25}Cu_{0.75}$(111) surface, H could not be adsorbed on the Ir_3 hollow site (Figure 5A, data in yellow). This is because the lattice constant of the surface is overcompressed due to the higher Cu percentage, leading to a misalignment of *d*-electrons among surface Ir atoms. It is also worth noting that H atoms could be adsorbed at the 3-fold hollow site of Ir_1Cu_2 instead of migrating to the Ir atop site (Figure 5B); this behavior is in contrast to some previously studied bimetallics (e.g., PtAu and IrAg) that show "untunable" H-binding behavior.[21,60,61] Compared to some other alloys that display both strong and weak adsorption capacities (e.g., PdAu and RhAu),[60] the differences among the three Ir-related triatomic ensembles are relatively small, suggesting overall weaker tunability for H adsorption on the CuIr (111) alloy surface. Alloying more Cu with Ir generally increases the number of Cu_3 ensembles, which in turn binds to H too weakly by dilution of Ir-containing ensembles, resulting in a predicted lowering of the overall catalytic hydrogenation activity. This is consistent with the experimental observation that the average TOF decreases somewhat linearly with decreasing Ir composition (Figure 4). The nearly linear hydrogenation TOF trend with the increase of strong binding metal composition is similar to our previous theories and experiments studied for PtAu[61] and AgIr.[21]

In order to understand the selectivity of CRAL hydrogenation toward CROL, we next conducted more intensive DFT calculations to optimize the CRAL binding geometries and calculate their binding energies at the surfaces of CuIrNPs (Figure 6). Calculations on the CRAL hydrogenation thermodynamics on Ir (111) show that the initial hydrogenation at the γ-carbon of C═C bond is more favorable than the others (Figure S25), in good agreement with results shown in Figure 4 and a previous study.[21] As seen in Figure 6, On small Ir ensembles alloyed with Cu (e.g., Ir_1 and Ir_2), binding of CRAL through C═C bonding at the Ir sites was found to be significantly more favorable, leading to a greater probability of C═C bond hydrogenation versus C═O; this trend is in direct agreement with the experimental observations here, and in previous studies.[21] At Ir_3 ensembles, the binding of CRAL was found to be further strengthened since both C═C and C═O can be coabsorbed (Figure 6A). The favorable binding of CRAL at Ir-related sites through adsorbing the C═C bond is independent of the Ir composition of the NPs, indicating that Ir-related sites are less able to tune the BUAL:CROL selectivity and BUAL is the major product obtained from these sites. This also matches with our previous combined experimental and theoretical studies.[21]

It has been confirmed in prior in situ spectroscopic studies that transition metal oxide supports such as Co_3O_4 and CeO_2, can improve the selectivity of C═O hydrogenation by stabilizing the C═O adsorption at the transition metal oxide-NP surfaces.[56,63] To evaluate the effect of Co_3O_4 support in this study, an Ir nanorod was next modeled on a Co_3O_4(110) support, with different numbers of doped Cu atoms at the metallic-oxide interface to simulate CuIr nanoclusters (Figure 6B). For the first time, adsorption of small molecules on large systems of NP and Co_3O_4 slabs was calculated and fully studied. It can be seen that with 0, 1, or 2 Cu atoms at the interface of Co_3O_4 and NPs, the binding of CRAL through C═O shows binding energies of −2.28, −2.15, and −2.35 eV, respectively, which are stronger than the binding energies of CRAL through C═O on any of the NP-based Ir_1 and Ir_2 sites (−1.54 and −1.51 eV, respectively; Figure 6A). Although CRAL cannot bind on Cu_3 site, DFT calculations show that the interface of Co_3O_4 and Cu_3 sites can still adsorb crotonaldehyde molecules via the C═O moiety with a favorable binding energy of −1.84 eV. Taken together, these theoretical results infer that Co_3O_4 stabilizes the adsorption of CRAL, and the overall observed reaction selectivity is derived by competition between direct C═C hydrogenation on the NP surfaces and C═O hydrogenation at the interface of Co_3O_4 and the NPs, the latter of which is largely insensitive to the Cu:Ir ratio. All these predictions are in good agreement with our experimental results observed in Figure 4. Due to the tremendous computational cost for the kinetic computation with these systems, we have not included the energy barrier calculation for the reactions.

■ CONCLUSIONS

In summary, stabilizer-free, ultrasmall CuIrNPs (~2 nm) were prepared in ethylene glycol media using a simple, one-pot microwave-assisted method. The structures of the NPs were elucidated with PXRD, XPS, ICP-OES, and HAADF-STEM. Hydroxide was found to facilitate the coreduction of Cu^{2+} and Ir^{3+} and the formation of Cu−Ir alloy NPs that are sufficiently stabilized by Cl^- and OH^- ions without the requirement for additional bulky organic capping agents, which greatly benefits their subsequent utilization as heterogeneous catalysts. $Cu_xIr_{(100-x)}$ supported in mesoporous Co_3O_4 showed similar

DOI: 10.1021/acs.chemmater.9b04138
Chem. Mater. 2019, 31, 10225−10235

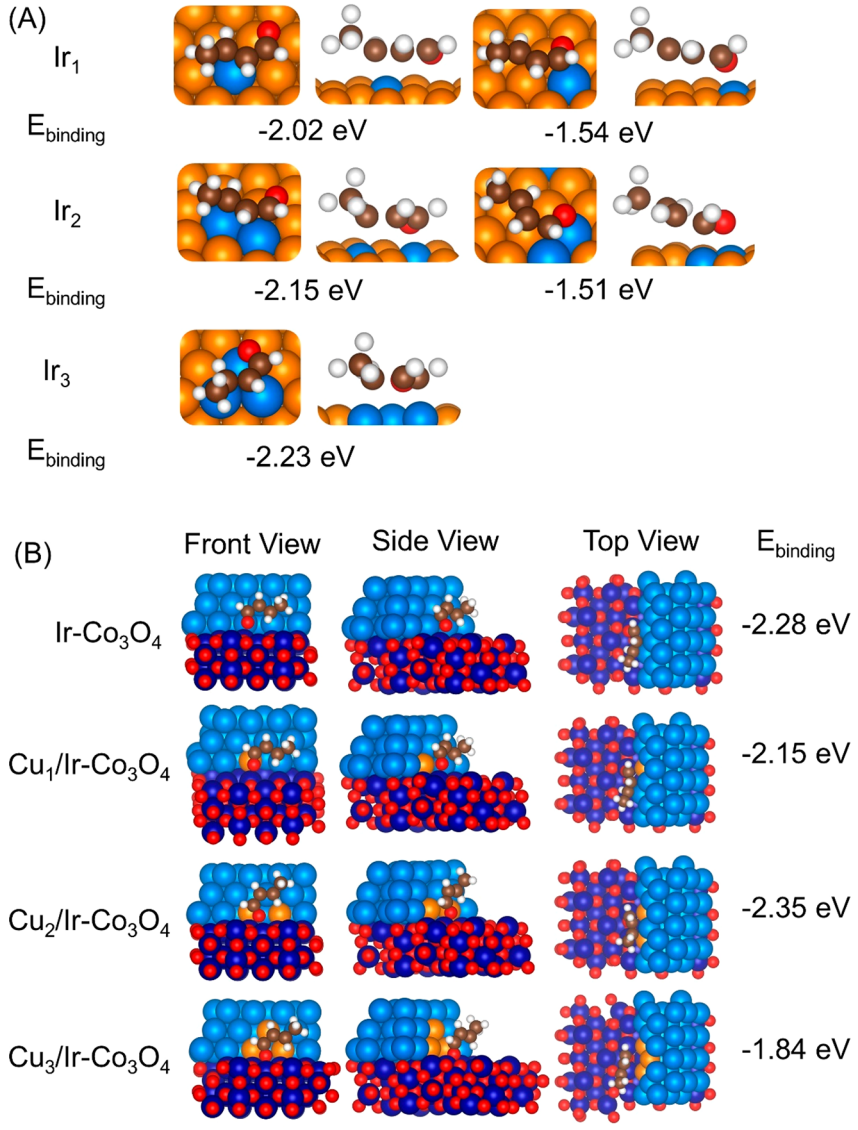

Figure 6. DFT-optimized binding geometries of crotonaldehyde at (A) CuIr surface ensembles and (B) CuIr nanorod supported on Co_3O_4(110). $E_{binding}$ is the calculated crotonaldehyde binding energy. Light blue, orange, white, brown, red, and deep blue spheres represent Ir, Cu, H, C, O, and Co, respectively.

catalytic selectivities to pure Ir NPs in the selective vapor-phase hydrogenation of crotonaldehyde, with appreciable selectivities toward the target unsaturated alcohol product. The observed trends in catalytic activity and selectivity were explained by DFT studies, which suggest that the surfaces of Cu−Ir nanoalloys both show H-binding tunability and also benefit from the adsorption-directing ability of Co_3O_4 as a support.

EXPERIMENTAL SECTION

Materials. Iridium trichloride ($IrCl_3{\cdot}xH_2O$, 100%; Johnson Matthey), copper(II) chloride dihydrate ($CuCl_2{\cdot}2H_2O$, reagent grade; Aldrich), ethylene glycol ($\{CH_2OH\}_2$, 99.8%; Fisher Scientific), poly(vinylpyrrolidone) (PVP, $\langle M_w \rangle$ = 58 000; Alfa Aesar), sodium hydroxide (NaOH, Fisher Scientific), copper(II) acetylacetonate ($Cu(acac)_2$, 97%; Aldrich), copper(II) bromide ($CuBr_2$, 99%; Aldrich), copper(II) perchlorate hexahydrate ($Cu(ClO_4)_2{\cdot}6H_2O$, 98%; Aldrich), copper acetate monohydrate ($Cu(OAc)_2{\cdot}H_2O$, Aldrich; 98%), crotonaldehyde (C_4H_8O, 99.5%, Aldrich), tetraethyl orthosilicate (TEOS, 98%; Acros Organics), poly(ethylene glycol)-block-poly(propylene glycol)-block-poly(ethylene glycol) (P123; Aldrich), cobalt(II) nitrate hexahydrate ($Co(NO_3)_2{\cdot}6H_2O$, 98%; Alfa Aesar) were used as-received. All other reagents and solvents (analytical grade) were used without further purification.

Synthesis of $Cu_xIr_{(100-x)}$NPs. Under continuous N_2 flow, 14 mL EG and 1 mL 0.25 M NaOH EG solution were heated to 125 °C in a Mars 5 Microwave Digestor, to which 5 mL EG solution containing 0.05 mmol $CuCl_2{\cdot}2H_2O$ and 0.05 mmol $IrCl_3$ was injected at a rate of 20 mL·min^{-1}. The mixture was heated for another 30 min before reaction was stopped by cooling the flask in an ice−water bath. The as-prepared NPs can be used directly for preparation of catalysts. Other purification methods are described in detail in the Results and Discussion section.

Synthesis of *m*-Co_3O_4 and $Cu_xIr_{(100-x)}$/*m*-Co_3O_4. SBA-15 was prepared according to the previous method and was used as the hard template.[64] In short, 2.78 g P123 was dissolved in 50 mL 0.3 M HCl aqueous solution at room temperature. After complete dissolution of P123, 5 g TEOS was added dropwise, and the mixture was stirred at 35 °C for 24 h. Then the mixture was sealed in a Nalgene PP vessel and heated at 100 °C for 24 h. The obtained slurry was separated by vacuum filtration and washed with DI-H_2O. A 5 h calcination (1.5 °C·min^{-1} ramp rate) was used to remove polymer.

DOI: 10.1021/acs.chemmater.9b04138
Chem. Mater. 2019, 31, 10225−10235

For the preparation of mesoporous Co_3O_4, 0.2 g SBA-15 prepared using above method was added to a 2 mL ethanol solution of $Co(NO_3)_2{\cdot}6H_2O$ (0.8 M). After brief sonication, the mixture was stirred at room temperature for 1 h, before the mixture was transferred to an oven at 80 °C for the complete evaporation of ethanol. The composite was then heated at 200 °C for 10 h to decompose $Co(NO_3)_2$. This impregnation−decomposition step was repeated twice using the same amount of $Co(NO_3)_2{\cdot}6H_2O$. After calcining the product at 450 °C for 6 h in furnace, SBA-15 template was removed by washing with 20 mL 2 M NaOH aqueous solution at 80 °C and *m*-Co_3O_4 was recovered by centrifugation.

$Cu_xIr_{(100-x)}$NPs/*m*-Co_3O_4 catalyst was prepared by adding $Cu_xIr_{(100-x)}$NPs dispersed in EG to *m*-Co_3O_4 dispersed in EtOH. The mixture was stirred for 24 h and separated by centrifugation. After being washed by copious EtOH, the catalyst obtained was dried under vacuum.

Physical Characterizations. Powder X-ray diffraction (PXRD) patterns of the $Cu_xIr_{(100-x)}$NPs was collected on Rigaku R-Axis Spider Diffractometer (40 kV and 40 mA) and Agilent Super Nova diffractometer (50 kV and 25 mA) equipped with an AtlasS2 CCD. Both diffractometers are equipped with Cu Kα sources (λ = 1.5405 Å). Transmission electron microscopy (TEM) images were collected on a FEI Tecnai Transmission Electron microscope operating at 80 kV and a JEOL 2010F Transmission Electron Microscope operating at 200 kV. TEM samples were prepared by drop-casting ethanol solutions of NPs on a copper grid (200 mesh Cu/Formvar; Ted Pella, Inc.) and allowing it to dry at room temperature. 2D-EDS mapping and line scan measurements were conducted on a JEOL 2010F Transmission Electron Microscope operating at 200 kV. Samples were prepared by drop-casting ethanol solutions of NPs on a nickel grid (CF200-Ni; Electron Microscopy Sciences, Inc.). X-ray photoelectron spectroscopy (XPS) were performed on a Kratos X-ray Photoelectron Spectrometer with monochromatic Al Kα source (1486.7 eV). Inductively coupled plasma optical emission spectrometry (ICP-OES) samples were prepared by digesting $Cu_xIr_{(100-x)}$NPs or catalysts in Teflon vessels at 200 °C for 2 h in CEM MARS 5 digestion oven. The digestion solution is a mixture of 1:3 (v:v) 30 wt % H_2O_2/12 M HCl.

Catalytic Tests. In a typical crotonaldehyde hydrogenation, around 30 mg $Cu_xIr_{(100-x)}$NPs/*m*-Co_3O_4 catalyst was mixed first with 250 mg acid-washed and precalcinated sand before loaded to a U-shaped reactor on a D3-prorosity frit. The reactor was heated to 70 °C under an atmosphere of H_2/He for 1 h to activate the catalyst. A bubbler containing crotonaldehyde was placed in an ice−water bath. H_2/He flew the bubbler and carried the saturated vapor of substrate through the catalyst bed. The product was directly introduced to a HP Agilent 6890 GC equipped with a 15 m Restex Stabiliwax column and FID.

Computational Section. All the density functional theory (DFT) calculations were performed using the Vienna Ab Initio Simulation Package (VASP). Electron correlation was described using the generalized gradient approximation (GGA) method with the Perdew−Burke−Ernzerhof (PBE) functional.[65] The projector augmented-wave method was employed to describe the core electrons.[66,67] Kohn−Sham wave functions were expanded in a plane wave basis for the description of valence electrons.[68] The energy cutoffs for H and CRAL binding systems were respectively set as 300 and 400 eV. Geometries were considered relaxed when the force (per atom) was below 0.01 eV/Å. A (3 × 3 × 1) Monkhorst−Pack *k*-point mesh and Gamma point were employed for the Brillouin zone sampling of the calculations on CuIr(111) and Ir−Co_3O_4, respectively.[69,70] The Tkatchenko and Scheffler method was used to provide van der Waals corrections to all the calculations in this study.[71] Spin-polarization and DFT+*U* method (U_{eff} = 3.3 eV) were employed for all the calculations with Co_3O_4.

All H binding energies on CuIr surfaces were calculated on the (111) surface of the 4-layer (4 × 4) slab. For each slab model, the top two layers were allowed to relax while the bottom two layers were kept fixed in the bulk positions. For the modeling of Cu_xIr_{1-x} alloy, ten alloy configurations were generated randomly. For the calculation of H binding energy, four different triatomic ensembles (Cu_3, Ir_1Cu_2, Ir_2Cu_1, and Ir_3) were selected as the initial adsorption sites of H. From all the random configurations, ten H binding sites were randomly sampled and calculated at each ensemble. The H_2 molecule (in vacuum) was selected as the reference of H binding energy. All the CRAL binding energies were calculated with the reference energy of CRAL in vacuum. The Ir−Co_3O_4 system was modeled with an Ir nanorod (2 × 4, 3 × 4, and 4 × 4 Ir in the topmost, middle, and bottom nanorod layers, respectively) supported on a Co_3O_4(110) surface (A termination). The CRAL was modeled to be adsorbed at the (111) surface of the nanorod.

■ ASSOCIATED CONTENT

Supporting Information

The Supporting Information is available free of charge at https://pubs.acs.org/doi/10.1021/acs.chemmater.9b04138.

Detailed experimental methods, further PXRD patterns, TEM images, XPS results for the $Cu_xIr_{(100-x)}$NPs, TEM images for the supports and composite catalysts, and additional catalysis information (PDF)

■ AUTHOR INFORMATION

Corresponding Authors

*E-mail: henkelman@utexas.edu (G.H.).
*E-mail: smh@cm.utexas.edu for (S.M.H.).

ORCID

Karalee Jarvis: 0000-0002-3560-0239
Graeme Henkelman: 0000-0002-0336-7153
Simon M. Humphrey: 0000-0001-5379-4623

Present Address

[‖]School of Chemistry, University of Bristol, Bristol, BS8 1TH, U.K.

Notes

The authors declare no competing financial interest.

■ ACKNOWLEDGMENTS

The authors thank Dr. Vincent M. Lynch (X-ray), Dr. Hugo Celio (XPS) and Dr. Dwight Romanovicz (TEM) for analytical assistance. Funding for this work was provided by the National Science Foundation under Grant No. CHE-1807847 and the Welch Foundation (F-1738, S.M.H. & F-1841, G.H.).

■ DEDICATION

[†]In Celebration of the 65[th] Birthday of our Colleague and Mentor, Prof. Richard M. Crooks.

■ REFERENCES

(1) Agarwal, N.; Freakley, S. J.; McVicker, R. U.; Althahban, S. M.; Dimitratos, N.; He, Q.; Morgan, D. J.; Jenkins, R. L.; Willock, D. J.; Taylor, S. H.; Kiely, C. J.; Hutchings, G. J. Aqueous Au-Pd Colloids Catalyze Selective CH_4 Oxidation to CH_3OH with O_2 under Mild Conditions. *Science* **2017**, *358*, 223−227.

(2) Huang, X.; Zhao, Z.; Cao, L.; Chen, Y.; Zhu, E.; Lin, Z.; Li, M.; Yan, A.; Zettl, A.; Wang, Y. M.; Duan, X.; Mueller, T.; Huang, Y. High-Performance Transition Metal-Doped Pt_3Ni Octahedra for Oxygen Reduction Reaction. *Science* **2015**, *348*, 1230−1234.

(3) Zhang, H.; Jin, M.; Xia, Y. Enhancing the Catalytic and Electrocatalytic Properties of Pt-Based Catalysts by Forming Bimetallic Nanocrystals with Pd. *Chem. Soc. Rev.* **2012**, *41*, 8035−8049.

(4) Rodríguez-González, B.; Burrows, A.; Watanabe, M.; Kiely, C. J.; Liz-Marzán, L. M. Multishell Bimetallic AuAg Nanoparticles:

DOI: 10.1021/acs.chemmater.9b04138
Chem. Mater. 2019, 31, 10225−10235

Synthesis, Structure and Optical Properties. *J. Mater. Chem.* **2005**, *15*, 1755−1759.
(5) Mayer, M.; Scarabelli, L.; March, K.; Altantzis, T.; Tebbe, M.; Kociak, M.; Bals, S.; García de Abajo, F. J.; Fery, A.; Liz-Marzán, L. M. Controlled Living Nanowire Growth: Precise Control Over the Morphology and Optical Properties of AgAuAg Bimetallic Nanowires. *Nano Lett.* **2015**, *15*, 5427−5437.
(6) Yang, P.; Jin, S. Y.; Xu, Q. Z.; Yu, S. H. Decorating PtCo Bimetallic Alloy Nanoparticles on Graphene as Sensors for Glucose Detection by Catalyzing Luminol Chemiluminescence. *Small* **2013**, *9*, 199−204.
(7) Gong, J.; Zhou, T.; Song, D.; Zhang, L.; Hu, X. Stripping Voltammetric Detection of Mercury(II) Based on a Bimetallic Au-Pt Inorganic-Organic Hybrid Nanocomposite Modified Glassy Carbon Electrode. *Anal. Chem.* **2010**, *82*, 567−573.
(8) Chen, M.; Kumar, D.; Yi, C. W.; Goodman, D. W. The Promotional Effect of Gold in Catalysis by Palladium-Gold. *Science* **2005**, *310*, 291−293.
(9) Kim, D.; Resasco, J.; Yu, Y.; Asiri, A. M.; Yang, P. Synergistic Geometric and Electronic Effects for Electrochemical Reduction of Carbon Dioxide Using Gold−Copper Bimetallic Nanoparticles. *Nat. Commun.* **2014**, *5*, 4948.
(10) Slanac, D. A.; Hardin, W. G.; Johnston, K. P.; Stevenson, K. J. Atomic Ensemble and Electronic Effects in Ag-Rich AgPd Nanoalloy Catalysts for Oxygen Reduction in Alkaline Media. *J. Am. Chem. Soc.* **2012**, *134*, 9812−9819.
(11) Zhang, J.; Yang, H.; Fang, J.; Zou, S. Synthesis and Oxygen Reduction Activity of Shape-Controlled Pt_3Ni Nanopolyhedra. *Nano Lett.* **2010**, *10*, 638−644.
(12) Zhang, J.; Fang, J. A General Strategy for Preparation of Pt 3d-Transition Metal (Co, Fe, Ni) Nanocubes. *J. Am. Chem. Soc.* **2009**, *131*, 18543−18547.
(13) Sra, A. K.; Schaak, R. E. Synthesis of Atomically Ordered AuCu and $AuCu_3$ Nanocrystals from Bimetallic Nanoparticle Precursors. *J. Am. Chem. Soc.* **2004**, *126*, 6667−6672.
(14) Sun, S.; Murray, C. B.; Weller, D.; Folks, L.; Moser, A. Monodisperse FePt Nanoparticles and Ferromagnetic FePt Nanocrystal Superlattices. *Science* **2000**, *287*, 1989−1992.
(15) Shevchenko, E. V.; Talapin, D. V.; Rogach, A. L.; Kornowski, A.; Haase, M.; Weller, H. Colloidal Synthesis and Self-Assembly of $CoPt_3$ Nanocrystals. *J. Am. Chem. Soc.* **2002**, *124*, 11480−11485.
(16) Hu, X.; Lin, C.; Wei, L.; Hong, C.; Zhang, Y.; Zhuang, N. High Electrocatalytic Performance of Graphene Nanoribbon Supported PtAu Nanoalloy for Direct Ethanol Fuel Cell and Theoretical Analysis of Anti-CO Poisoning. *Electrochim. Acta* **2016**, *187*, 560−566.
(17) Yang, J.; Su, M.; Zhao, Y.; Li, J.; Li, M.; Huang, T. Facile Microwave-Assisted Synthesis of Concave Octahedral Pt-Cu Alloy Nanocrystals and their Electrocatalytic Properties. *ChemNanoMat* **2018**, *4*, 909−913.
(18) Chatterjee, D.; Shetty, S.; Muller-Caspary, K.; Grieb, T.; Krause, F. F.; Schowalter, M.; Rosenauer, A.; Ravishankar, N. Ultrathin Au-Alloy Nanowires at the Liquid-Liquid Interface. *Nano Lett.* **2018**, *18*, 1903−1907.
(19) de la Hoz, A.; Diaz-Ortiz, A.; Moreno, A. Microwaves in Organic Synthesis. Thermal and non-Thermal Microwave Effects. *Chem. Soc. Rev.* **2005**, *34*, 164−178.
(20) Baghbanzadeh, M.; Carbone, L.; Cozzoli, P. D.; Kappe, C. O. Microwave-Assisted Synthesis of Colloidal Inorganic Nanocrystals. *Angew. Chem., Int. Ed.* **2011**, *50*, 11312−11359.
(21) Guo, H.; Li, H.; Jarvis, K.; Wan, H.; Kunal, P.; Dunning, S. G.; Liu, Y.; Henkelman, G.; Humphrey, S. M. Microwave-Assisted Synthesis of Classically Immiscible Ag-Ir Alloy Nanoparticle Catalysts. *ACS Catal.* **2018**, *8*, 11386−11397.
(22) García, S.; Zhang, L.; Piburn, G. W.; Henkelman, G.; Humphrey, S. M. Microwave Synthesis of Classically Immiscible Rhodium-Silver and Rhodium-Gold Alloy Nanoparticles: Highly Active Hydrogenation Catalysts. *ACS Nano* **2014**, *8*, 11512−11521.
(23) Heuer-Jungemann, A.; Feliu, N.; Bakaimi, I.; Hamaly, M.; Alkilany, A.; Chakraborty, I.; Masood, A.; Casula, M. F.; Kostopoulou, A.; Oh, E.; et al. The Role of Ligands in the Chemical Synthesis and Applications of Inorganic Nanoparticles. *Chem. Rev.* **2019**, *119*, 4819−4880.
(24) Niu, Z.; Li, Y. Removal and Utilization of Capping Agents in Nanocatalysis. *Chem. Mater.* **2014**, *26*, 72−83.
(25) Deutsch, D. S.; Siani, A.; Fanson, P. T.; Hirata, H.; Matsumoto, S.; Williams, C. T.; Amiridis, M. D. FT-IR Investigation of the Thermal Decomposition of Poly(amidoamine) Dendrimers and Dendrimer-Metal Nanocomposites Supported on Al_2O_3 and ZrO_2. *J. Phys. Chem. C* **2007**, *111*, 4246−4255.
(26) Lee, I.; Morales, R.; Albiter, M. A.; Zaera, F. Synthesis of Heterogeneous Catalysts with Well-shaped Platinum Particles to Control Reaction Selectivity. *Proc. Natl. Acad. Sci. U. S. A.* **2008**, *105*, 15241−15246.
(27) Liu, Z.; Shamsuzzoha, M.; Ada, E. T.; Reichert, W. M.; Nikles, D. E. Synthesis and Activation of Pt Nanoparticles with Controlled Size for Fuel Cell Electrocatalysts. *J. Power Sources* **2007**, *164*, 472−480.
(28) Li, D. G.; Wang, C.; Tripkovic, D.; Sun, S. H.; Markovic, N. M.; Stamenkovic, V. R. Surfactant Removal for Colloidal Nanoparticles from Solution Synthesis: The Effect on Catalytic Performance. *ACS Catal.* **2012**, *2*, 1358−1362.
(29) Fu, G.; Wu, K.; Lin, J.; Tang, Y.; Chen, Y.; Zhou, Y.; Lu, T. One-Pot Water-Based Synthesis of Pt-Pd Alloy Nanoflowers and Their Superior Electrocatalytic Activity for the Oxygen Reduction Reaction and Remarkable Methanol-Tolerant Ability in Acid Media. *J. Phys. Chem. C* **2013**, *117*, 9826−9834.
(30) Rioux, R. M.; Song, H.; Grass, M.; Habas, S.; Niesz, K.; Hoefelmeyer, J. D.; Yang, P.; Somorjai, G. A. Monodisperse Platinum Nanoparticles of Well-Defined Shape: Synthesis, Characterization, Catalytic Properties and Future Prospects. *Top. Catal.* **2006**, *39*, 167−174.
(31) Crespo-Quesada, M.; Andanson, J.-M.; Yarulin, A.; Lim, B.; Xia, Y.; Kiwi-Minsker, L. UV-Ozone Cleaning of Supported Poly(vinylpyrrolidone)-Stabilized Palladium Nanocubes: Effect of Stabilizer Removal on Morphology and Catalytic Behavior. *Langmuir* **2011**, *27*, 7909−7916.
(32) Wu, J. B.; Zhang, J. L.; Peng, Z. M.; Yang, S. C.; Wagner, F. T.; Yang, H. Truncated Octahedral Pt_3Ni Oxygen Reduction Reaction Electrocatalysts. *J. Am. Chem. Soc.* **2010**, *132*, 4984−4985.
(33) Ansar, S. M.; Ameer, F. S.; Hu, W.; Zou, S.; Pittman, C. U.; Zhang, D. Removal of Molecular Adsorbates on Gold Nanoparticles Using Sodium Borohydride in Water. *Nano Lett.* **2013**, *13*, 1226−1229.
(34) Luo, M.; Hong, Y.; Yao, W.; Huang, C.; Xu, Q.; Wu, Q. Facile Removal of Polyvinylpyrrolidone (PVP) Adsorbates from Pt Alloy Nanoparticles. *J. Mater. Chem. A* **2015**, *3*, 2770−2775.
(35) Choi, S.-I.; Xie, S.; Shao, M.; Odell, J. H.; Lu, N.; Peng, H.-C.; Protsailo, L.; Guerrero, S.; Park, J.; Xia, X.; Wang, J.; Kim, M. J.; Xia, Y. Synthesis and Characterization of 9 nm Pt−Ni Octahedra with a Record High Activity of 3.3 A/mg_{Pt} for the Oxygen Reduction Reaction. *Nano Lett.* **2013**, *13*, 3420−3425.
(36) Yang, X.; Roling, L.; Vara, M.; Elnabawy, A.; Zhao, M.; Hood, Z.; Bao, S.; Mavrikakis, M.; Xia, Y. Synthesis and Characterization of Pt-Ag Alloy Nanocages with Enhanced Activity and Durability toward Oxygen Reduction. *Nano Lett.* **2016**, *16*, 6644−6649.
(37) Huang, L.; Zhang, X.; Wang, Q.; Han, Y.; Fang, Y.; Dong, S. Shape-Control of Pt-Ru Nanocrystals: Tuning Surface Structure for Enhanced Electrocatalytic Methanol Oxidation. *J. Am. Chem. Soc.* **2018**, *140*, 1142−1147.
(38) Aliaga, C.; Park, J. Y.; Yamada, Y.; Lee, H. S.; Tsung, C.-K.; Yang, P.; Somorjai, G. A. Sum Frequency Generation and Catalytic Reaction Studies of the Removal of Organic Capping Agents from Pt Nanoparticles by UV-Ozone Treatment. *J. Phys. Chem. C* **2009**, *113*, 6150−6155.
(39) Li, H.; Luo, L.; Kunal, P.; Bonifacio, C. S.; Duan, Z.; Yang, J. C.; Humphrey, S. M.; Crooks, R. M.; Henkelman, G. Oxygen Reduction Reaction on Classically Immiscible Bimetallics: A Case Study of RhAu. *J. Phys. Chem. C* **2018**, *122*, 2712−2716.

DOI: 10.1021/acs.chemmater.9b04138
Chem. Mater. 2019, 31, 10225−10235

(40) Bartholomew, C. H. Mechanisms of Catalyst Deactivation. *Appl. Catal., A* **2001**, *212*, 17−60.
(41) Wang, Y.; Ren, J. W.; Deng, K.; Gui, L. L.; Tang, Y. Q. Preparation of Tractable Platinum, Rhodium, and Ruthenium Nanoclusters with Small Particle Size in Organic Media. *Chem. Mater.* **2000**, *12*, 1622−1627.
(42) Carpenter, M. K.; Moylan, T. E.; Kukreja, R. S.; Atwan, M. H.; Tessema, M. M. Solvothermal Synthesis of Platinum Alloy Nanoparticles for Oxygen Reduction Electrocatalysis. *J. Am. Chem. Soc.* **2012**, *134*, 8535−8542.
(43) Liu, Y.; Chen, L.; Cheng, T.; Guo, H.; Sun, B.; Wang, Y. Preparation and Application in Assembling High-Performance Fuel Cell Catalysts of Colloidal PtCu Alloy Nanoclusters. *J. Power Sources* **2018**, *395*, 66−76.
(44) Choi, S.-I.; Xie, S.; Shao, M.; Odell, J. H.; Lu, N.; Peng, H.-C.; Protsailo, L.; Guerrero, S.; Park, J.; Xia, X.; Wang, J.; Kim, J. M.; Xia, Y. Synthesis and Characterization of 9 nm Pt−Ni Octahedra with a Record High Activity of 3.3 A/mg_{Pt} for the Oxygen Reduction Reaction. *Nano Lett.* **2013**, *13*, 3420−3425.
(45) Wang, F.; Kusada, K.; Wu, D.; Yamamoto, T.; Toriyama, T.; Matsumura, S.; Nanba, Y.; Koyama, M.; Kitagawa, H. Solid-Solution Alloy Nanoparticles of the Immiscible Iridium-Copper System with a Wide Composition Range for Enhanced Electrocatalytic Applications. *Angew. Chem., Int. Ed.* **2018**, *57*, 4505−4509.
(46) Tsuji, M.; Hikino, S.; Tanabe, R.; Matsunaga, M.; Sano, Y. Syntheses of Ag/Cu Alloy and Ag/Cu Alloy Core Cu Shell Nanoparticles Using a Polyol Method. *CrystEngComm* **2010**, *12*, 3900−3908.
(47) Freakley, S. J.; Ruiz-Esquius, J.; Morgan, D. J. The X-ray Photoelectron Spectra of Ir, IrO_2 and $IrCl_3$ Revisited. *Surf. Interface Anal.* **2017**, *49*, 794−799.
(48) Schrader, I.; Warneke, J.; Neumann, S.; Grotheer, S.; Swane, A. A.; Kirkensgaard, J. J. K.; Arenz, M.; Kunz, S. Surface Chemistry of "Unprotected" Nanoparticles: A Spectroscopic Investigation on Colloidal Particles. *J. Phys. Chem. C* **2015**, *119*, 17655−17661.
(49) Gilroy, K. D.; Ruditskiy, A.; Peng, H.-C.; Qin, D.; Xia, Y. Bimetallic Nanocrystals: Syntheses, Properties, and Applications. *Chem. Rev.* **2016**, *116*, 10414−10472.
(50) Snyder, J.; McCue, I.; Livi, K.; Erlebacher, J. Structure/Processing/Properties Relationships in Nanoporous Nanoparticles as Applied to Catalysis of the Cathodic Oxygen Reduction Reaction. *J. Am. Chem. Soc.* **2012**, *134*, 8633−8645.
(51) Gong, M.; Fu, G.; Chen, Y.; Tang, Y.; Lu, T. Autocatalysis and Selective Oxidative Etching Induced Synthesis of Platinum-Copper Bimetallic Alloy Nanodendrites Electrocatalysts. *ACS Appl. Mater. Interfaces* **2014**, *6*, 7301−7308.
(52) Fievet, F.; Lagier, J. P.; Blin, B.; Beaudoin, B.; Figlarz, M. Homogeneous and Heterogeneous Nucleations in the Polyol Process for the Preparation of Micron and Submicron Size Metal Particles. *Solid State Ionics* **1989**, *32*−*33*, 198−205.
(53) Chen, L.-J.; Wan, C.-C.; Wang, Y.-Y. Chemical Preparation of Pd Nanoparticles in Room Temperature Ethylene Glycol System and its Application to Electroless Copper Deposition. *J. Colloid Interface Sci.* **2006**, *297*, 143−150.
(54) Claus, P. Selective Hydrogenation of α,β-Unsaturated Aldehydes and Other C═O and C═C Bonds Containing Compounds. *Top. Catal.* **1998**, *5*, 51−62.
(55) Zanella, R.; Louis, C.; Giorgio, S.; Touroude, R. Crotonaldehyde Hydrogenation by Gold Supported on TiO_2: Structure Sensitivity and Mechanism. *J. Catal.* **2004**, *223*, 328−339.
(56) Kennedy, G.; Melaet, G.; Han, H.; Ralston, W. T.; Somorjai, G. A. In Situ Spectroscopic Investigation into the Active Sites for Crotonaldehyde Hydrogenation at the Pt Nanoparticle-Co_3O_4 Interface. *ACS Catal.* **2016**, *6*, 7140−7147.
(57) Chiu, M. E.; Watson, D. J.; Kyriakou, G.; Tikhov, M. S.; Lambert, R. M. Tilt the molecule and change the chemistry: mechanism of S-promoted chemoselective catalytic hydrogenation of crotonaldehyde on Cu(111). *Angew. Chem., Int. Ed.* **2006**, *45*, 7530−7534.
(58) Reyes, P.; Aguirre, M. C.; Pecchi, G.; Fierro, J. L. G. Crotonaldehyde Hydrogenation on Ir Supported Catalysts. *J. Mol. Catal. A: Chem.* **2000**, *164*, 245−251.
(59) Wang, Y.; Choi, S.-I.; Zhao, X.; Xie, S.; Peng, H.-C.; Chi, M.; Huang, C. Z.; Xia, Y. Polyol Synthesis of Ultrathin Pd Nanowires via Attachment-Based Growth and Their Enhanced Activity towards Formic Acid Oxidation. *Adv. Funct. Mater.* **2014**, *24*, 131−139.
(60) Li, H.; Shin, K.; Henkelman, G. Effects of Ensembles, Ligand, and Strain on Adsorbate Binding to Alloy Surfaces. *J. Chem. Phys.* **2018**, *149*, 174705.
(61) Luo, L.; Duan, Z.; Li, H.; Kim, J.; Henkelman, G.; Crooks, R. M. Tunability of the Adsorbate Binding on Bimetallic Alloy Nanoparticles for the Optimization of Catalytic Hydrogenation. *J. Am. Chem. Soc.* **2017**, *139*, 5538−5546.
(62) Kunal, P.; Li, H.; Dewing, B. L.; Zhang, L.; Jarvis, K.; Henkelman, G.; Humphrey, S. M. Microwave-Assisted Synthesis of Pd_xAu_{100-x} Alloy Nanoparticles: A Combined Experimental and Theoretical Assessment of Synthetic and Compositional Effects upon Catalytic Reactivity. *ACS Catal.* **2016**, *6*, 4882−4893.
(63) Yang, X.; Mueanngern, Y.; Baker, Q. A.; Baker, L. R. Crotonaldehyde Hydrogenation on Platinum-Titanium Oxide and Platinum-Cerium Oxide Catalysts: Selective C═O Bond Hydrogen Requires Platinum Sites Beyond the Oxide-Metal Interface. *Catal. Sci. Technol.* **2016**, *6*, 6824−6835.
(64) Rumplecker, A.; Kleitz, F.; Salabas, E.-L.; Schüth, F. Hard Templating Pathways for the Synthesis of Nanostructured Porous Co_3O_4. *Chem. Mater.* **2007**, *19*, 485−496.
(65) Perdew, J. P.; Burke, K.; Ernzerhof, M. Generalized Gradient Approximation Made Simple. *Phys. Rev. Lett.* **1996**, *77*, 3865−3868.
(66) Blöchl, P. E. Projector Augmented-Wave Method. *Phys. Rev. B: Condens. Matter Mater. Phys.* **1994**, *50*, 17953−17979.
(67) Kresse, G.; Joubert, D. From Ultrasoft Pseudopotentials to the Projector Augmented-Wave Method. *Phys. Rev. B: Condens. Matter Mater. Phys.* **1999**, *59*, 1758−1775.
(68) Kohn, W.; Sham, L. Self-Consistent Equations Including Exchange and Correlation Effects. *Phys. Rev.* **1965**, *140*, A1133−A1138.
(69) Monkhorst, H. J.; Pack, J. D. Special Points for Brillouin-Zone Integrations. *Phys. Rev. B* **1976**, *13*, 5188−5192.
(70) Methfessel, M.; Paxton, A. T. High-Precision Sampling for Brillouin-Zone Integration in Metals. *Phys. Rev. B: Condens. Matter Mater. Phys.* **1989**, *40*, 3616−3621.
(71) Tkatchenko, A.; Scheffler, M. Accurate Molecular Van der Waals Interactions from Ground State Electron Density and Free-Atom Reference Data. *Phys. Rev. Lett.* **2009**, *102*, 073005.

DOI: 10.1021/acs.chemmater.9b04138
Chem. Mater. 2019, 31, 10225−10235